Magnetic frustration control through tunable stereochemically driven disorder in entropy-stabilized oxides

Peter B. Meisenheimer, Logan D. Williams, Suk Hyun Sung, Jiseok Gim, Padraic Shafer, George N. Kotsonis, Jon-Paul Maria, Morgan Trassin, Robert Hovden, Emmanouil Kioupakis, and John T. Heron

Phys. Rev. Materials **3**, 104420 — Published 28 October 2019

DOI: 10.1103/PhysRevMaterials.3.104420

Magnetic Frustration Control Through Tunable Stereochemically-Driven Disorder in Entropy-Stabilized Oxides

Peter B. Meisenheimer[1], Logan D. Williams[1], Suk Hyun Sung[1], Jiseok Gim[1], Padraic Shafer[2], George N. Kotsonis[3], Jon-Paul Maria[3], Morgan Trassin[4], Robert Hovden[1], Emmanouil Kioupakis[1] & John T. Heron*[,1]

[1] University of Michigan, Department of Materials Science and Engineering, 2300 Hayward St, Ann Arbor, MI, USA, 48109

[2] Lawrence Berkeley National Laboratory, Advanced Light Source, One Cyclotron Rd, Berkeley, CA, USA, 94720

[3] Pennsylvania State University, Department of Materials Science and Engineering, 221 Steidle Building, University Park, PA, USA 16802

[4] ETH Zurich, Laboratory for Multifunctional Materials, Vladimir-Prelog-Weg 1-5/10, Zürich, Switzerland, 8093

*Correspondence to: jtheron@umich.edu

Abstract

Entropy-stabilized oxides possess a large configurational entropy that allows for the unique ability to include typically immiscible concentrations of species in new configurations. Particularly in oxides, where the physical behavior is strongly correlated to stereochemistry and electronic structure, entropic stabilization creates a unique platform to tailor the interplay of extreme structural and chemical disorder to realize unprecedented functionalities. Here, we control stereochemically-driven structural disorder in single crystalline, rocksalt, (MgCoNiCuZn)O-type entropy-stabilized oxides through the incorporation of Cu^{2+} cations. We harness the disorder to tune the degree of glassiness in the antiferromagnetic magnetic structure. Structural distortions driven by the Jahn-Teller effect lead to a difference in valence on the Co cation sites, which extends to dilution and disorder of the magnetic lattice. A spin glass model reveals that the fractional spin ordering of the magnetic lattice can be tuned by ~65%. These findings demonstrate entropy-stabilization as a new tool for control of functional phenomena.

I. INTRODUCTION

Highly disordered, chemically homogeneous, single phase metallic and ceramic solid solutions have attracted significant interest in recent years due to the observation of enhanced physical properties and new emergent phases [1–5]. In high-entropy and entropy-stabilized materials, crystals with typically 5 or more species, the large configurational entropy is thought to be a critical factor in the stabilization of the phase [6–9]. While this concept has been proposed in metal alloys several years ago, only recently has it been extended to ceramics where the configurational entropy is created by chemically disordering the cation sublattice [10–12]. Particularly for oxides, pioneering experimental work has demonstrated the emergence of a homogenous single phase at a critical entropy and that the critical temperature varies with the configurational entropy [12]. These, so-called, entropy-stabilized oxides (ESOs) enable an unprecedented new degree of chemical control in materials, as the technique can be used to incorporate typically immiscible concentrations of cationic species in an atypical coordination. As the properties of oxides are strongly correlated to their stereochemistry and electronic structure [13–16], ESOs thus present the opportunity to tune charge [17], lattice [18–20], and spin [21] disorders to new extremes in a single-phase, single-crystalline material. In fact, remarkable properties such as glass-like thermal conductivity [17] and colossal physical properties [21–23] have been observed, yet the contributions of disorder in structure and chemistry to these properties, along with their interplay and tunability, remains to be uncovered.

In a conventional binary rock salt oxide, such as MgO, NiO, or CoO, the cation species sit on octahedrally-coordinated sites. The (MgCoNiCuZn)O-type rock salt ESOs studied here, however, are expected to deviate from this ideal configuration due to the presence of disordering species. Specifically, Cu^{2+} cations will tend to undergo a tetragonal distortion from an octahedral configuration in order to break the e_g orbital degeneracy present in a d^9 system (i.e. the Jahn-Teller (JT) effect). In (MgCoNiCuZn)O, however, the Cu^{2+} cations are forced into the rock salt structure, in competition with the JT effect, leading to a frustration of the atomic positions around the site. This competition is expected to significantly impact the functional properties and disorder [21]. Here we find that the crystalline lattice of (MgCoNiCuZn)O ESO thin films is structurally distorted by this stereochemical frustration and drives a change in the fraction of 3+/

2+ Co cation oxidation states. We find that this structurally driven change in oxidation state corresponds to the disorder in magnetic structure. Our results reveal that the unique characteristics of ESO single crystal thin films can be tuned to large degrees to control of structural and chemical disorder and engineer magnetic functional phenomena.

To this end, copper variant $(Mg_{0.25(1-x)}Co_{0.25(1-x)}Ni_{0.25(1-x)}Cu_xZn_{0.25(1-x)})O$ (x = 0.11, 0.17, 0.20, 0.24, 0.27) and cobalt variant $(Mg_{0.25(1-x)}Co_xNi_{0.25(1-x)}Cu_{0.25(1-x)}Zn_{0.25(1-x)})O$ (x = 0.20, 0.27, 0.33) ESO thin films were investigated to probe the interplay of chemical and structural disorder on magnetic order. These compositions were chosen systematically because Cu^{2+} cations will tend to distort the octahedral site, creating a mechanism of structural disorder. This effect has been observed both in bulk [24], from diffraction analysis, and previously in thin film form [18] using extended X-ray absorption fine structure. Because these active sites are spread across the crystal in large concentrations (1/5 of cation sites in an equimolar, 5-component ESO), we hypothesize that this will create a concerted effect and drive structural frustrations across the whole system [24,25]. In contrast, Co^{2+} prefers octahedral coordination, minimizing structural disorder, and changes the average magnetic moment significantly (~1.6 to 1.9 μ_B cation^{-1}) [21]. Bulk $(Mg_{0.2}Co_{0.2}Ni_{0.2}Cu_{0.2}Zn_{0.2})O$ was previously shown, through neutron and AC susceptibility, to be antiferromagnetic (AFM) with a degree of glassines manifested in the sluggish paramagnetic (PM)/AFM transition and temperature dependence of the peak in susceptibility. This material was also shown to be AFM as a thin film, possessing a large ferromagnetic (FM)/AFM exchange coupling [21] when capped with permalloy (Py) in a heterostructure. As exchange bias is especially sensitive to magnetic frustration [26,27] and provides an ideal method for studying magnetic disorder in these systems since the magnetic disorder of the oxide can be read out through effects on the exchange interaction. Through this novel technique, we show that the Cu^{2+} concentration can be directly correlated to lattice, charge, and spin disorder in ESO thin films, while the structure retains a high degree of crystallinity and phase purity.

II. EXPERIMENTAL

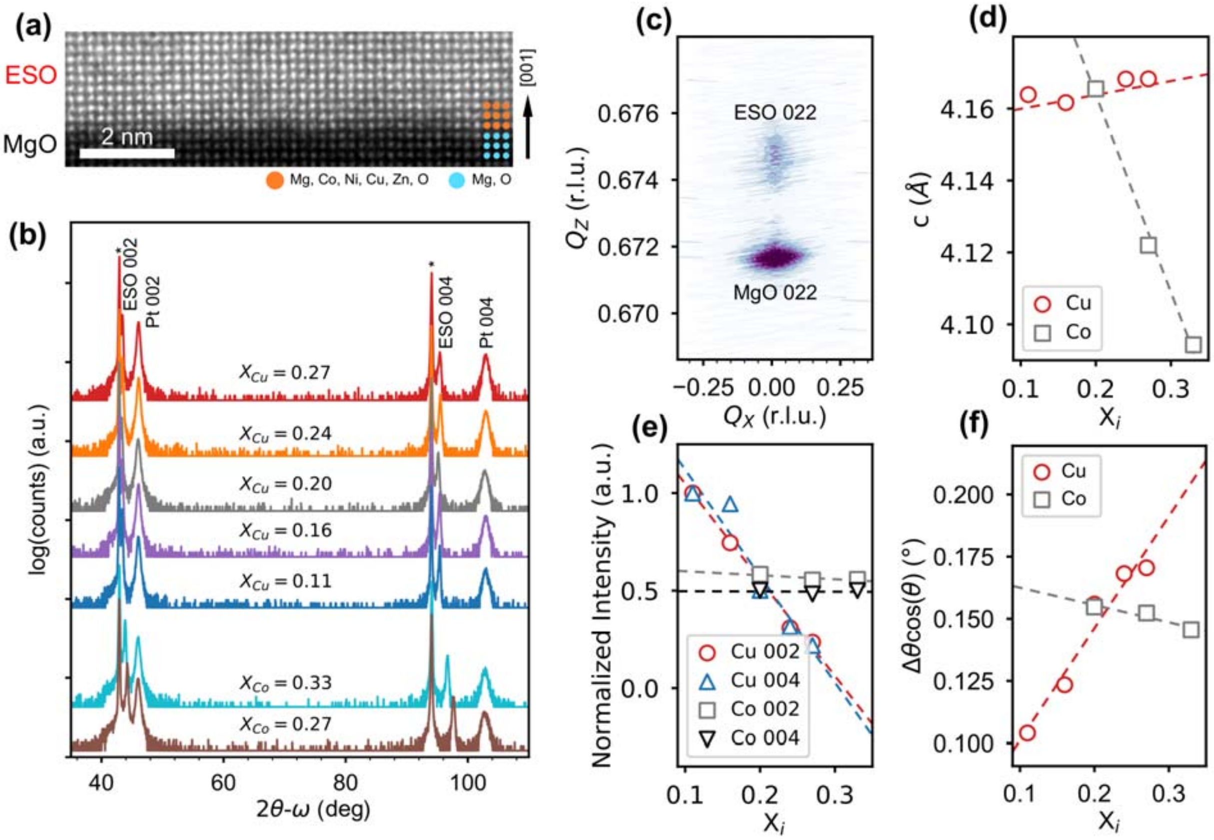

FIG. 1. Control of structural disorder through stereochemical frustration. **(a)** Atomic resolution cross-section HAADF-STEM micrograph of 90 nm thick ESO film on MgO substrate. **(b)** $2\theta - \omega$ XRD spectra of Cu and Co variant ESO thin films. Only the 002 and 004 peaks from the ESO film are present, showing phase purity and epitaxy. * indicates MgO 002 and 004 substrate peaks. **(c)** Reciprocal space map of equimolar, X = 0.20, ESO, showing that the film is clamped to the substrate in the Q_X direction (in-plane). **(d)** Out-of-plane lattice constants of the Cu variant and Co variant ESO films determined using Cohen's method. **(e)** Normalized peak intensities of the ESO 002 and 004 peaks, showing a decrease in the peak intensity with increasing Cu. **(f)** Full-width at half-max ($\Delta\theta$) of the 002 peaks in **(a)**, deconvolved with peak position, showing a significant increase in the peak width with increasing Cu concentration and a small decrease with Co composition.

Previous work has shown that the dominant exchange in ESO thin films is antiferromagnetic [21,28,29], thus we deposited FM/ESO bilayers in order to probe the exchange effects and evolution of magnetic order with chemical and structural disorder in the ESO films. 80 nm thick single crystalline epitaxial films of $(Mg_{0.25(1-x)}Co_{0.25(1-x)}Ni_{0.25(1-x)}Cu_xZn_{0.25(1-x)})O$ (X_{Cu} = 0.11, 0.17, 0.20, 0.24, 0.27) (hereafter referred to as Cu variant) and

$Mg_{0.25(1-x)}Co_xNi_{0.25(1-x)}Cu_{0.25(1-x)}Zn_{0.25(1-x)})O$ (X_{Co} = 0.20, 0.27, 0.33) (Co variant) were deposited on (001)-oriented MgO single crystal substrates. All ESO films show excellent crystalline quality and phase purity by high-angle annular dark-field scanning transmission electron microscopy (HAADF-STEM) and X-ray diffraction [30] (**Figs. 1(a-d)** and **Sup. Figs. S1 and S2**). The targeted composition was confirmed by X-ray photoelectron spectroscopy (**Sup. Fig. S3**) to within the measurement resolution and the film surface roughness was determined to be ~100 pm RMS or less by atomic force microscopy. The ESO films were capped with 3 nm of Py as a FM layer, and ~20 nm of Pt to prevent oxidation of the Py [21]. We measure a saturation magnetization of 800 emu cm^{-3} for our permalloy films, agreeing with the bulk value.

III. RESULTS AND DISCUSSION

A. Tuning of Structural Disorder

In the typical Jahn-Teller distortion of Cu^{2+}, the axial bond will elongate and the basal bonds will contract in order to break the octahedral symmetry and remove the degeneracy of the unpaired electron in the e_g orbital [25]. This, naturally, gives rise to a bimodal distribution of bond lengths and a tetragonal distortion of the cation site. From our XRD spectra, we observe this structural distortion as a function of Cu composition. The peak intensities of the 002 and 004 film diffraction peaks, normalized to the substrate peak intensity and then scaled, show a linear decrease with increasing concentration of Cu (**Fig. 1(e)**), consistent with an increasing tetragonal or monoclinic distortion of the lattice that breaks symmetry about the 002 peak [24,25]. Additionally, the peak width increases with the concentration of Cu (**Fig. 1(f)**), implying a large degree of correlated disorder in the system [31]. In contrast, the relative intensity and peak widths of the 002 peaks for the Co variant films remain invariant (**Fig. 1(e, f)**). Here, the broadening of peaks is consistent with atom displacements that are larger near an impurity atom in a randomly dilute solid solution (i.e. "Huang scattering" [32]). Uncorrelated displacements (known as Debye-Waller scattering [33,34]) and uncorrelated chemical disorder (known as Laue monotonic scattering [35]) do not broaden Bragg peaks in the same fashion, therefore we are able to directly tie and tune the degree of global structural disorder in the material to the concentration of the Jahn-Teller species.

Atomic-resolution HAADF STEM of the ESO film [30] (**Fig. 1a and Sup. Fig. S2**) confirms single crystal growth and one-to-one atomic epitaxy at an atomically sharp interface with the substrate. We observe that crystal symmetry is broken through a contraction, relative to the substrate, of the lattice along the growth direction (tetragonal distortion) as seen by an expansion of the 00n lattice peaks in Fourier space. This change in lattice constant is correlated to Cu concentration, as the out-of-plane lattice constant increases measurably when comparing the 27% Cu sample to the 11% Cu sample. The Fourier transform was measured over a 20 nm^2 field of view, and in this sense, is a local representation of the film structure.

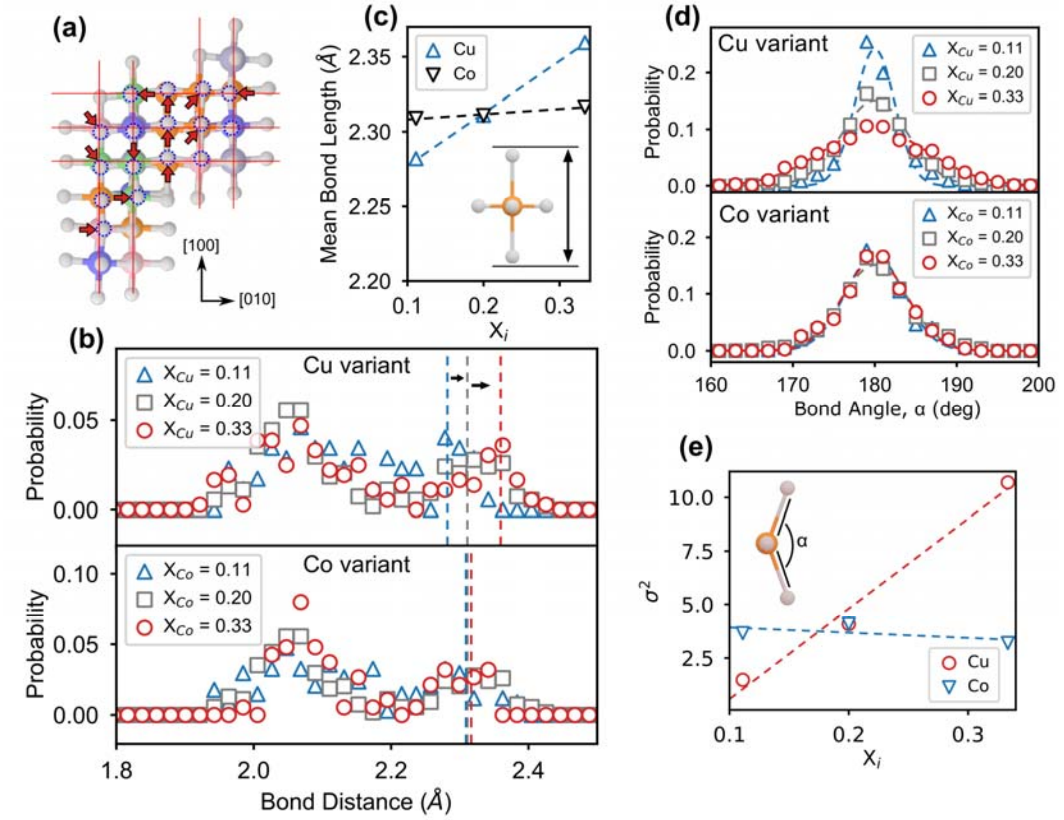

FIG. 2. Simulated bond length disorder in compositionally variant ESOs. **(a)** 94-atom supercell of Cu-rich ESO relaxed using DFT. Ideal planes of atoms are overlaid in red, highlighting the structural distortions (emphasized by arrows) most clearly on the oxygen anion sites (shown in grey). The Cu cations are shown in orange. **(b)** Histograms of bond lengths on the Cu-cation sites for $X_{Cu,Co}$ = 0.11, 0.20, 0.33 ESOs, demonstrating the characteristic double peak of a Jahn-Teller distorted cation. **(c)** Axial bond length of the Cu site in Cu variant (Cu) and Co variant (Co) ESO. As the concentration of Cu is increased in the material, we observe an increase in the length of the z (extended)-axis on the Cu cation site, implying that the degree of distortion is sensitive to the local environment

about the Cu site and the total concentration of Cu. **(d)** Histogram of cation-anion-cation bond angles, α, for Cu variant and Co variant ESOs calculated from DFT. **(e)** Variance (σ^2) of the Gaussian fits to the data in **(d)**. As the concentration of Cu cations is increased, the variance of the calculated bond angle changes significantly in a linear fashion while the Co variant samples remain approximately constant.

From density functional theory (DFT) calculations of our Cu variant ESOs, we can observe this structural distortion on an atomic scale. The relaxed atomic coordinates (**Fig. 2(a)**) show a large spatial deviation from the perfect rock salt structure. The histogram of the bond lengths in our simulated ESO supercells exhibits the characteristic bimodal distribution of the Jahn-Teller effect (**Fig. 2(b)**). Interestingly, we also observe a shift in the peak length of the extended axial bond with increasing concentration of Cu (**Fig. 2(b, c)**). In the case of varying Co concentration, the peak-length shift is negligible. This shows that Cu is responsible for the structural distortion. Additionally, our analysis demonstrates that the disorder-driving sites are working in a concerted manner, agreeing with our observation in **Fig. 1** of a concerted symmetry breaking.

Further, our first-principles calculations of the structures for the Cu and Co variant ESOs also show a significant variation in bond angle (up to nearly 20°) that is correlated to increasing Cu incorporation (**Fig. 2(d, e)**). As the concentration of Cu in the supercell is increased, the variance of the bond angle distribution increases sharply, by 10x over the relatively small compositional space. This linear trend also agrees with the compositional disorder observed in our XRD measurement from the FWHM of the film diffraction peaks [31] (**Fig. 1(f)**). The bond length and bond angle disorder can influence cation charge state (through strain) and magnetic interaction, as superexchange is particularly susceptible to changes in orbital overlap [36–39] and coordination. Thus, we probe the evolution of the cation charge and AFM character by X-ray absorption and X-ray linear dichroism.

B. X-ray Absorption

It has been previously observed that charge disorder can be fundamentally tied into structural effects in ESOs [17,22,24]. From X-ray absorption spectroscopy (XAS) measurements, we observe a significant fraction of low spin Co^{3+} in the oxide for all compositions (**Fig. 3(a)**). As the concentration of Cu is increased, we observe an approximately linear change in the ratio of high spin Co^{2+} to low spin Co^{3+} (**Fig. 3(b)**). At higher concentrations of Cu, there is a smaller fraction of Co^{2+}. As the only process variable changing in our experiment is the concentration of Cu sites, and thus the structural homogeneity that is proportional to Cu inclusion, we posit that that the observed change in charge state is influenced by the Cu^{2+} JT effect. We find that the charge state of the other cations remains invariant to within experimental resolution [30] (**Sup. Fig. S4**).

This effect can also be tied directly, through X-ray linear dichroism (XLD), to the strength of the magnetic interaction in the ESO. Best data fits suggest that Co^{3+} is in the low spin state, which is nonmagnetic, and thus Cu additions, which promote a growing Co^{3+} fraction, decrease in the strength of the AFM character of the system (**Fig. 3(b)**) as the fraction of Co^{2+} decreases. Collectively, structural frustration from changing bond angles, magnetic dilution due to conversion of Co^{2+} to Co^{3+}, and glassy AFM in bulk samples [28], motivates an exploration of FM/AFM exchange bias, as this is known to be particularly susceptible to frustration of the magnetic lattice [21,40].

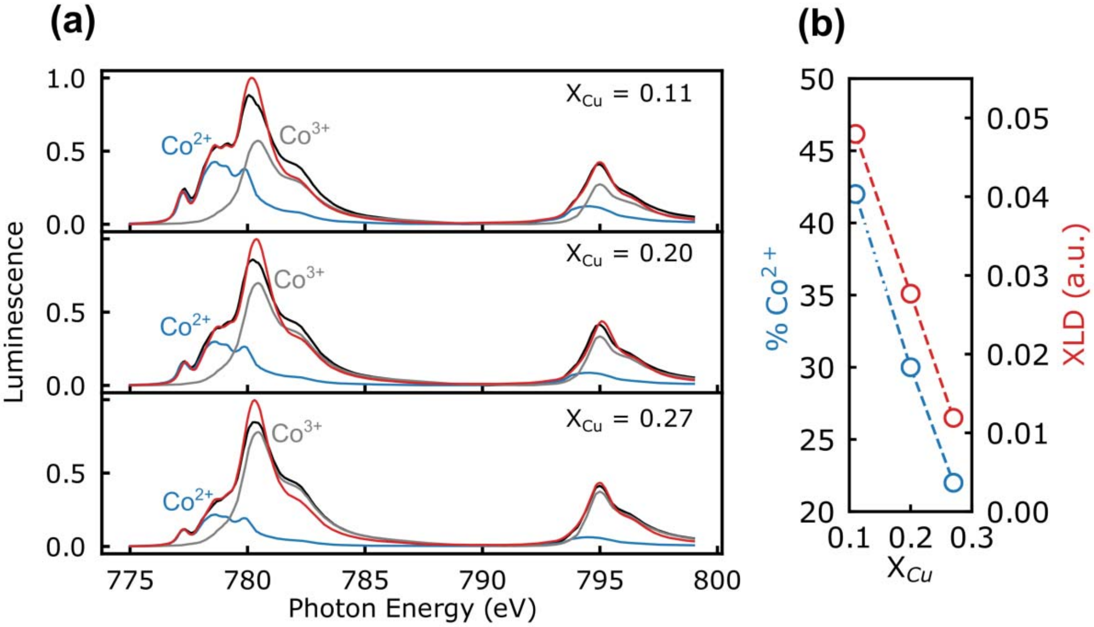

FIG. 3. X-ray absorption. **(a)** Evolution of Co XAS lineshapes from X-ray luminescence in the Cu-series samples showing a gradual change in ratio of high spin Co^{2+} (blue) to low spin Co^{3+} (grey) proportional to the Cu content of

the sample. Measured spectra are shown in red, with fits in black. Spectra were fit to a linear combination of the Co^{2+} (high spin), Co^{3+} (low spin), and Co^{3+} (high spin) peaks taken from ref. [41]. The Co3+ fraction was eliminated as a result of the fitting and is therefore not shown. **(b)** Plot of Co^{2+} fraction from the coefficients of the linear combination in (a) alongside measured X-ray linear dichroism (XLD) from samples in (a). As the Cu concentration of the samples is increased, the fraction of the 2+ oxidation state decreases proportionally. Additionally, the dichroic signal on the Co cation sites decreases with the same trend. XLD was measured at room temperature and 80 K, above and below the Néel temperature respectively to observe structural and magnetic components.

C. Magnetic Analysis

FM/AFM exchange bias is known to be dependent on magnetic frustration of the AFM layer [26,27]. The spin glass model for exchange bias [42,43] argues that frustrated magnetic moments at the FM/AFM interface couple to the FM magnetization, creating the characteristic bias field. The pinned surface moments are hard and slow to move, resulting in the exchange bias itself, and the degree of disorder, directly proportional to the thickness of the glassy layer, is dependent on the intrinsic order and anisotropy of the magnetic lattice in the AFM [43]. This model can be expressed as an energy balance using the system of equations [42]:

$$\frac{H\mu_0 M t_F}{-Jf} sin(\theta - \beta) + \frac{1-f}{f} sin\big(2(\beta - \gamma)\big) + sin(\beta - \alpha) = 0$$

$$\frac{K_{AF} t_{AF}}{fJ} sin(2\alpha) - sin(\beta - \alpha) = 0.$$

Where H is the applied magnetic field, M and t_F are the magnetization and thickness of the FM layer, J is the interfacial exchange energy, f is the fractional spin ordering, θ is the angle between the applied field and the anisotropy axis of the FM, β is the angle between the FM magnetization and the FM easy axis, γ is the angle between the applied field and the preferred orientation of the glassy layer, α is the angle between the surface magnetization of the AFM and the anisotropy axis of the AFM, and K_{AF} and t_{AF} are the anisotropy energy and thickness of the AFM layer.

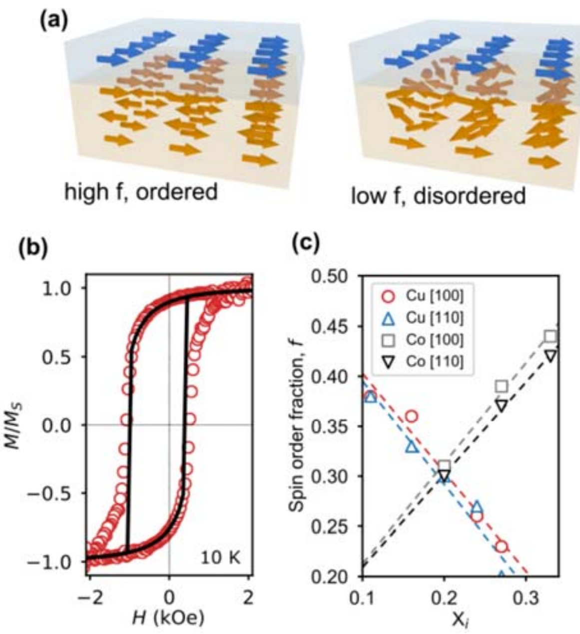

FIG. 4. Control of magnetic disorder. **(a)** Schematic to illustrate the spin lattice of the antiferromagnetic layer when it is highly ordered (high f, left) and highly disordered (low f, right). For simplicity the FM layer is depicted here in its saturated state. As the magnetic lattice of the AFM is frustrated, changes can be read out through the FM layer. **(b)** Normalized magnetic moment versus field for the equimolar composition at 10 K. Experimental data is shown with the open circles and the fit from the model is shown as a solid line. Fit corresponds to an R^2 parameter of 0.987. The sample was biased by cooling from 300 K in a 1 T magnetic field. **(c)** Spin ordering parameter f as a function of Cu and Co concentrations. As the concentration of Cu (red, blue) is increased, the magnetic lattice is increasingly disordered and as we increase the concentration of Co (grey, black), the degree of frustration decreases. Data is extracted from magnetic hysteresis loops taken at 10 K. Dashed lines are provided as guides to the eye.

To study magnetic disorder, we probe the parameter f, the fractional spin ordering at the interface, where f = 1 is the maximum ordering and f = 0 is the maximum disorder. This is shown schematically in **Fig. 4(a)**. For reference, the well-studied Co/CoO exchange bias system has shown a spin ordering of f = 0.8 [42]. Numerically solving the system of equations for the unknowns J, f, γ, and α (assuming $\theta, \beta = 0$) and fitting to experimental magnetometry data taken at 10 K, we obtain a quantitative measure of the magnetic disorder in our ESO exchange biased heterostructures. Fitting was accomplished by globally minimizing the goodness-of-fit (R^2) from ~10^5 points in parameter space (see **APPENDIX C**). An example of a fit hysteresis loop is shown in **Fig. 4(b)**. In all cases here, α is small (~0°) and R^2 >0.94. As the concentration of Cu is increased in the oxides, we observe an approximately linear decrease in the spin ordering parameter, f (**Fig. 4(c)**). Our results indicate that the concentration of Cu is directly proportional to the degree of spin frustration in the magnetic lattice. This linear proportionality agrees with our results from XLD (**Fig. 3(b)**), which shows a linear decrease in the AFM character of the cation sites as Cu concentration is increased. Our observed value of f is small, even compared with the canonical spin glass, CuMn, studied in reference [44] ($f = 0.65$).

We posit that the significant magnetic disorder in the system is driven by the magnetic dilution and the superexchange interactions where tightly bound electrons in the oxide system are more easily frustrated by structural deformation than those of a delocalized, metallic antiferromagnet [45,46]. Further, our experimental results correlate with the observed change in the bond angle distribution from theoretical calculations, providing evidence for this assertion, that the variance in cation-oxygen-metal bond angle is a primary driver of magnetic frustration in ESO systems. This is also mediated by a difference in valence on the Co cation sites, driven by Jahn-Teller structural distortions, which results in dilution and disorder of the magnetic lattice. Additionally, inclusion of Co should result in the inverse effect as Co has a negligible influence on the structural disorder while increasing the number of AFM sites. Indeed, as the concentration of Co is increased in the Co variant samples, we observe an approximately linear increase in f, corresponding to a decrease in the spin disorder. This is complemented by XAS data showing that the Co^{2+}/Co^{3+} ratio becomes approximately invariant with Co incorporation, indicating that it primarily the change in average cation moment, rather than oxidation state, which is driving the observed trend.

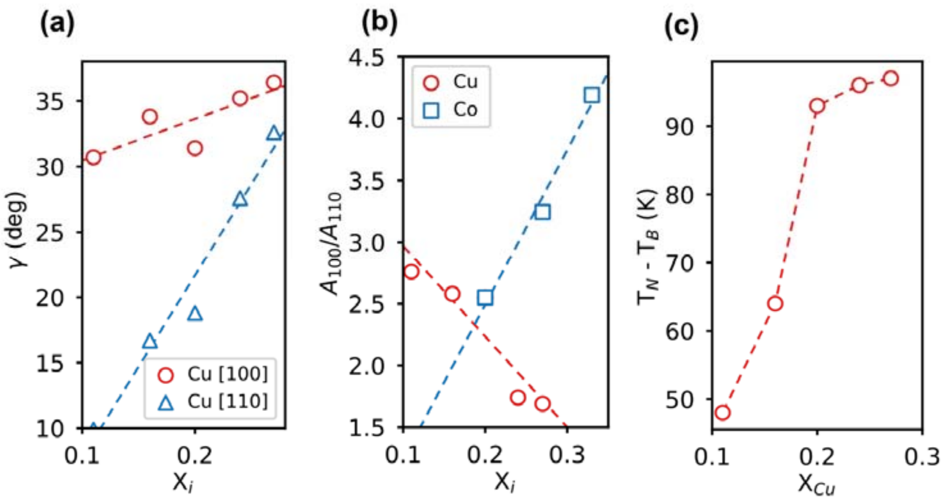

FIG. 5. Anisotropy parameters of the fits to magnetic data. (**a**), angle, γ, between the applied field and the preferred axis of the spin glass as a function of composition. As the concentration of Cu is increased, the difference between γ along the [100] and [110] directions approaches 0, showing that the magnetic lattice is tending toward isotropy with increasing Cu. **(b),** Ratio between anisotropy energies for the [100] and [110] directions. As Cu concentration is increased, the ratio approaches 1 and the system tends towards isotropy. As Co concentration is increased, the anisotropy becomes stronger and [110] becomes the preferred easy axis. Dashed lines in each plot are guides to the eye. **(c),** Plot of the difference between T_N and T_B reveals the sluggishness of the transition, as a function of Cu concentration, indicating increasing glassiness in the ESO as Cu incorporation is increased.

This frustration can also be seen in the γ parameter extracted from the model, corresponding to the difference between the preferred orientation of the glassy layer and the measurement direction, similar to an enforced easy axis in the spin glass. As the concentration of Cu is increased in the oxide, the difference in γ along the [100] and [110] crystallographic axes approaches 0 (**Fig. 5(a)**). This indicates that the driving force for a preferred axis is weaker and the magnetic lattice becomes more isotropic with increasing Cu. Indeed, the anisotropy energies also show this, as the ratio A_{100}/A_{110}, the energies along the [100] and [110] directions respectively (calculated from $A_i = \int_0^{Ms} H(M)dM$), approaches 1 with increasing Cu incorporation, showing that the ESO becomes more magnetically isotropic (**Fig. 5(b)**). Our data agree with our theoretically calculated bond angles in the ESO, as the bond angle is increasingly disordered in a linear fashion by the inclusion of Cu^{2+} (**Fig. 2(e)**), and XAS data showing that the system becomes more magnetically dilute as Cu concentration increases.

Conversely, the ratio A_{100}/A_{110} increases with increasing Co inclusion, showing that spin frustration decreases and [110] becomes the easy axis. This agrees with previous results reported in ref. [21], as it was observed that the [110] axis becomes more favorable with increasing Co concentration. This is also in agreement with the magnetic structure observed in bulk experiments [28,29] of the equimolar composition where an average G-type order with the Néel vector along the [111] emerges below the Néel temperature of ~135 K.

Additionally, moment versus temperature curves, **Sup. Fig. S7**, show a large separation between T_N and T_B [30], revealing sluggish paramagnetic/AFM transitions as observed in glassy systems [47] and in bulk (MgCoNiCuZn)O [28,29]. The separation between these temperatures increases with increasing Cu concentration, illustrating that the system gets more frustrated with concentration (**Fig. 5(c)**) and providing further evidence of structurally driven glassiness. This observation is supported by the slow onset of the AFM state observed in bulk [28,29], as well as the broadening of the magnetic susceptibility peak from ref. [28] with the inclusion of increasingly frustrated cations.

IV. CONCLUSION

In conclusion, we have demonstrated that using entropy-stabilized oxides, a large tunability of magnetic disorder can be achieved through correlations in lattice, charge, and spin disorder. By tuning the degree of stereochemical frustration in the material, we can tune the structural disorder to drive oxidation state changes in magnetically active cations and create a disorder in the magnetic lattice.

ACKNOWLEDGEMENTS

This work was supported by IMRA America. This work was supported by NSF CAREER grant DMR-1847847. This work was funded in part by NSF grant No. DMR-0420785 (XPS) and NSF major research instrumentation grant No. DMR-1428226 (PPMS). Computational resources were provided by the DOE NERSC facility (DE-AC02-05CH11231) and NSF grant DMR-1810119. This research used resources of the Advanced Light Source, which is a DOE Office of

Science User Facility under contract no. DE-AC02-05CH11231. We acknowledge use of the NSF PARADIM facilities (DMR-1539918) at Cornell University. We thank the University of Michigan's Michigan Center for Materials Characterization, (MC)^2, for its assistance with XPS, as well as Prof. Lu Li and Dr. Ziji Xiang for their assistance with PPMS measurements. We thank Mike Waters for his assistance with the bond analysis of the DFT calculations.

APPENDIX A: Sample Deposition. Targets were prepared by mixing and grinding the constituent binaries (MgO (Alfa Aesar, 99.99%), CoO (Alfa Aesar, 99.99%), NiO (Alfa Aesar, 99.99%), CuO (Alfa Aesar, 99.99%), and ZnO (Alfa Aesar, 99.99%)), then pressing the composite powder at 70,000 psi and sintering at 1100 °C for 18 hours in an air atmosphere. 80 nm thick films were deposited at 300 °C in 50 mtorr of O_2 by ablation from a 248 nm KrF excimer laser fired at 6 Hz. A 3 nm Permalloy (Py) film was then deposited in vacuum at 40 °C and capped with ~20 nm of Pt to prevent oxidation.

2θ-ω and reflectometry scans were performed on a Rigaku Smartlab diffractometer equipped with 1.54 Å Cu Kα source and Ge-220 2-bounce monochromator. Reciprocal space maps (**Sup. Fig. S1**) were conducted using a chi-phi goniometer and a second Ge-220 2-bounce monochromator on the acquisition side.

High-angle annular dark-field scanning transmission electron microscopy (HAADF-STEM) was collected using FEI Titan Themis 300 operated at 300 keV with convergence semi-angle of 21.4 mrad. Electron energy loss spectroscopy (EELS) was performed with Gatan GIF Quantum K2 system at 0.25 eV/Ch dispersion. Cross-sectional TEM samples were focused ion beam (FIB) lifted out using FEI Nova 200 Nanolab SEM/FIB. (20 nm)^2 field of view Fast Fourier Transform (FFT) of substrate and film was taken from a single interfacial image. FFT peaks were analyzed by non-linear least square fitting 6-parameter 2D Gaussian to 002 and 200 peaks. $X_{cu} = 11\%$ shows (0.9 ± 0.3) % compression along 002 while $X_{cu} = 27\%$ shows smaller (0.4 ± 0.2) %. Errors were estimated from difference in 200 reciprocal lattice constants of substrate and film.

APPENDIX B: X-ray Absorption Spectroscopy. XA and X-ray linear dichroism (XLD) spectra were measured at the Advanced Light Source at Lawrence Berkeley National Laboratory on beamline 4.0.2. XA and XLD data were recorded at both room temperature and 80 K, above and below the Néel temperatures of the samples. Full spectra at 80 K are shown in **Sup. Fig. S4** [30]. Spectra were normalized over 8 scans per element, and data reported here shows the X-ray absorption that was calculated using luminescence yield collected from samples. This detection mode uses a photodiode to collect visible luminescence from the substrate (i.e., scintillator) to measure the intensity of X-rays transmitted through the film. X-ray absorption data were fit to a linear combination of reference spectra for Co^{2+}, Co^{3+} (low spin), and Co^{3+} (high spin) from ref. [41] using a basin-hopping optimization technique as implemented in Scipy for Python3. The Co^{3+} fraction was eliminated as a result of the fitting and is therefore not shown. Coefficients from this fit are reported as cation fractions.

All spectra were measured with linearly polarized x-rays; both horizontal and vertical polarizations were used. At every photon energy, absorption intensity is scaled to the flux of incoming x-rays. Spectra are normalized so that their polarization-averaged intensity ranges from "0" to "1", as shown in Fig. 3(a) and upper panels of Fig. S4. The XLD spectra in the lower panels of Fig. S4 are the difference of these normalized spectra that were measured with horizontal and vertical polarizations; i.e., XLD intensity = horizontal intensity – vertical intensity. The XLD values in Fig. 3(b) are the maximum values extracted from the corresponding Co XLD spectra in Fig. S4.

APPENDIX C: Magnetometry. Magnetic properties of the exchange bias heterostructures were examined using a Quantum Design Dynacool 14 T Physical Property Measurement System. Samples were cooled from 350 K to 10 K under a 2 T field applied along the measurement axis. Isothermal magnetic hysteresis loops were then taken in 25 K increments back up to 350 K. Moment versus temperature curves were taken by cooling the samples from 350 K to 5 K under 2 T (field cool) and 0 Oe (zero field cool), then measuring while warming to room temperature under a 50 Oe field to prevent demagnetization.

Use of the Radu model here is motivated by: 1) a sluggish AFM/PM transition has been observed in bulk [28,29], consistent with the phase having a glassy component. 2) Magnetic dilution is known to increase a glassy component in AFM systems (for instance CuMn alloys). 3) Such a strong correlation of structure, charge, and measured magnetic data agrees with our expectations. For instance, the disordered moments mediate the exchange coupling in the Radu model and result directly in the induced coercivity. Hysteresis loops were fit and magnetic parameters were extracted using numerical solutions to:

$$\frac{H\mu_0 M t_F}{-Jf} sin(\theta - \beta) + \frac{1-f}{f} sin\big(2(\beta - \gamma)\big) + sin(\beta - \alpha) = 0$$

$$\frac{K_{AF} t_{AF}}{fJ} sin(2\alpha) - sin(\beta - \alpha) = 0.$$

As calculated in the Python3 computing environment. Goodness of fit was determined using least-squares analysis of the fit to the hysteresis loop, calculated in the region from large positive field until switching, and large negative field until switching. Approximately 10^5 solutions are calculated across the entire parameter space in a course, evenly spaced, grid to minimize R^2. This is then done again using a finer grid of points about the previously calculated minimum. List of parameters and visualization of the fits is available in **Sup. Figs. S5 and S6** [30]. Anisotropy energies of the samples were calculated using the fits from above along the [100] and [110] crystallographic directions.

APPENDIX D: Density Functional Theory. DFT calculations were performed based on the projector augmented wave (PAW) method [48,49] using the Vienna *Ab initio* Simulation Package (VASP) [50–53]. Utilized pseudopotentials included 9, 2, 12, 10, 11, and 6 valence electrons for Co, Mg, Zn, Ni, Cu, and O respectively. A 900 eV plane-wave cutoff and Monkhorst-Pack kpoint grids with a density of at least 20 kpoints/Å^{-1} were used to obtain energy convergence of under 1 meV/atom. Ion relaxations with fixed lattice constants were performed using the functional of Perdew-Burke-Ernzerhof [54]. Forces on atoms were relaxed to within 1meV/Å. Random alloys were modeled using Special Quasi-random Structures (SQSs) generated with the Alloy Theoretic Automated Toolkit [55] taking into account pair correlations up to 6 Å. Supercells contained 24, 60, and 36 atoms for the 33% Cu and 33% Co, equimolar, and 11% Cu and 11% Co compositions, respectively. Structural data was assembled from SQSs that were relaxed using multiple magnetic configurations, including antiferromagnetic along (111) planes, ferromagnetic, and multiple random magnetic configurations. As sampling of roughly random alloy configurations produces structural probability distributions with clear trends based on composition, and the individual supercell distributions were qualitatively similar, the authors believe that the observed trends are real and expect them to be present in the physical system.

References

[1] M.-H. Tsai and J.-W. Yeh, Mater. Res. Lett. **2**, 107 (2014).
[2] D. B. Miracle, JOM 1 (2017).
[3] S. Praveen and H. S. Kim, Adv. Eng. Mater. **20**, 1700645 (n.d.).
[4] B. Gludovatz, A. Hohenwarter, D. Catoor, E. H. Chang, E. P. George, and R. O. Ritchie, Science **345**, 1153 (2014).
[5] F. Zhang, Y. Wu, H. Lou, Z. Zeng, V. B. Prakapenka, E. Greenberg, Y. Ren, J. Yan, J. S. Okasinski, X. Liu, Y. Liu, Q. Zeng, and Z. Lu, Nat. Commun. **8**, ncomms15687 (2017).
[6] J. W. Yeh, S. K. Chen, S. J. Lin, J. Y. Gan, T. S. Chin, T. T. Shun, C. H. Tsau, and S. Y. Chang, Adv. Eng. Mater. **6**, 299 (2004).
[7] Y. Zhang, Y. J. Zhou, J. P. Lin, G. L. Chen, and P. K. Liaw, Adv. Eng. Mater. **10**, 534 (2008).
[8] H. Huang, Y. Wu, J. He, H. Wang, X. Liu, K. An, W. Wu, and Z. Lu, Adv. Mater. **29**, 1701678 (2017).
[9] Y. P. Wang, B. S. Li, and H. Z. Fu, Adv. Eng. Mater. **11**, 641 (2009).
[10] J. Gild, M. Samiee, J. L. Braun, T. Harrington, H. Vega, P. E. Hopkins, K. Vecchio, and J. Luo, J. Eur. Ceram. Soc. **38**, 3578 (2018).
[11] J. Gild, Y. Zhang, T. Harrington, S. Jiang, T. Hu, M. C. Quinn, W. M. Mellor, N. Zhou, K. Vecchio, and J. Luo, Sci. Rep. **6**, 37946 (2016).
[12] C. M. Rost, E. Sachet, T. Borman, A. Moballegh, E. C. Dickey, D. Hou, J. L. Jones, S. Curtarolo, and J.-P. Maria, Nat. Commun. **6**, 8485 (2015).
[13] J. B. Goodenough, Prog. Solid State Chem. **5**, 145 (1971).
[14] M. Imada, A. Fujimori, and Y. Tokura, Rev. Mod. Phys. **70**, 1039 (1998).
[15] L. W. Martin, Y. H. Chu, and R. Ramesh, Mater. Sci. Eng. R Rep. **68**, 89 (2010).
[16] A. P. Ramirez, A. Hayashi, R. J. Cava, R. Siddharthan, and B. S. Shastry, Nature **399**, 333 (1999).
[17] J. L. Braun, C. M. Rost, M. Lim, A. Giri, D. H. Olson, G. N. Kotsonis, G. Stan, D. W. Brenner, J.-P. Maria, and P. E. Hopkins, Adv. Mater. **0**, 1805004 (n.d.).
[18] C. M. Rost, Z. Rak, D. W. Brenner, and J.-P. Maria, J. Am. Ceram. Soc. **100**, 2732 (n.d.).
[19] Zs. Rák, J.-P. Maria, and D. W. Brenner, Mater. Lett. **217**, 300 (2018).
[20] S. Sivakumar, E. Zwier, P. B. Meisenheimer, and J. T. Heron, JoVE J. Vis. Exp. e57746 (2018).
[21] P. B. Meisenheimer, T. J. Kratofil, and J. T. Heron, Sci. Rep. **7**, 13344 (2017).
[22] D. Berardan, S. Franger, A. K. Meena, and N. Dragoe, J Mater Chem A 9536 (2016).
[23] D. Berardan, S. Franger, D. Dragoe, A. K. Meena, and N. Dragoe, Phys. Status Solidi - Rapid Res. Lett. **10**, 328 (2016).
[24] D. Berardan, A. K. Meena, S. Franger, C. Herrero, and N. Dragoe, J. Alloys Compd. **704**, 693 (2017).
[25] D. P. Shoemaker and R. Seshadri, Phys. Rev. B **82**, 214107 (2010).
[26] Ch. Binek, A. Hochstrat, and W. Kleemann, J. Magn. Magn. Mater. **234**, 353 (2001).

[27] U. Nowak, K. D. Usadel, J. Keller, P. Miltényi, B. Beschoten, and G. Güntherodt, Phys. Rev. B **66**, 014430 (2002).

[28] M. P. Jimenez-Segura, T. Takayama, D. Bérardan, A. Hoser, M. Reehuis, H. Takagi, and N. Dragoe, Appl. Phys. Lett. **114**, 122401 (2019).

[29] J. Zhang, J. Yan, S. Calder, Q. Zheng, M. A. McGuire, D. L. Abernathy, Y. Ren, S. H. Lapidus, K. Page, H. Zheng, J. W. Freeland, J. D. Budai, and R. P. Hermann, Chem. Mater. **31**, 3705 (2019).

[30] See Supplemental Material at [URL will be inserted by publisher] for RSM, TEM, and XPS data shwoing film quality, full XAS spectra, visualizations of the fits to magnetometry curves, and example Néel and blocking temperatures

[31] D. A. Keen and A. L. Goodwin, Nature **521**, 303 (2015).

[32] Huang Kun and Mott Nevill Francis, Proc. R. Soc. Lond. Ser. Math. Phys. Sci. **190**, 102 (1947).

[33] I. Waller, Z. Für Phys. **17**, 398 (1923).

[34] P. Debye, Ann. Phys. **348**, 49 (1913).

[35] B. E. Warren, B. L. Averbach, and B. W. Roberts, J. Appl. Phys. **22**, 1493 (1951).

[36] X. Rocquefelte, K. Schwarz, and P. Blaha, Sci. Rep. **2**, 759 (2012).

[37] T. Shimizu, T. Matsumoto, A. Goto, T. V. Chandrasekhar Rao, K. Yoshimura, and K. Kosuge, Phys. Rev. B **68**, 224433 (2003).

[38] J. Snyder, J. S. Slusky, R. J. Cava, and P. Schiffer, Nature **413**, 48 (2001).

[39] A. P. Ramirez, in *Handb. Magn. Mater.* (Elsevier, 2001), pp. 423–520.

[40] J.-I. Hong, T. Leo, D. J. Smith, and A. E. Berkowitz, Phys. Rev. Lett. **96**, 117204 (2006).

[41] C. F. Chang, Z. Hu, H. Wu, T. Burnus, N. Hollmann, M. Benomar, T. Lorenz, A. Tanaka, H.-J. Lin, H. H. Hsieh, C. T. Chen, and L. H. Tjeng, Phys. Rev. Lett. **102**, 116401 (2009).

[42] F. Radu, A. Westphalen, K. Theis-Bröhl, and H. Zabel, J. Phys. Condens. Matter **18**, L29 (2006).

[43] F. Radu, A. Nefedov, J. Grabis, G. Nowak, A. Bergmann, and H. Zabel, J. Magn. Magn. Mater. **300**, 206 (2006).

[44] M. Ali, P. Adie, C. H. Marrows, D. Greig, B. J. Hickey, and R. L. Stamps, Nat. Mater. **6**, 70 (2007).

[45] I. S. Hagemann, P. G. Khalifah, A. P. Ramirez, and R. J. Cava, Phys. Rev. B **62**, R771 (2000).

[46] J. Karel, Y. N. Zhang, C. Bordel, K. H. Stone, T. Y. Chen, C. A. Jenkins, D. J. Smith, J. Hu, R. Q. Wu, S. M. Heald, J. B. Kortright, and F. Hellman, Mater. Res. Express **1**, 026102 (2014).

[47] J.-W. Cai, C. Wang, B.-G. Shen, J.-G. Zhao, and W.-S. Zhan, Appl. Phys. Lett. **71**, 1727 (1997).

[48] G. Kresse and D. Joubert, Phys. Rev. B **59**, 1758 (1999).

[49] P. E. Blöchl, Phys. Rev. B **50**, 17953 (1994).

[50] G. Kresse and J. Furthmüller, Phys. Rev. B **54**, 11169 (1996).

[51] G. Kresse and J. Hafner, Phys. Rev. B **47**, 558 (1993).

[52] G. Kresse and J. Hafner, Phys. Rev. B **49**, 14251 (1994).

[53] G. Kresse and J. Furthmüller, Comput. Mater. Sci. **6**, 15 (1996).

[54] J. P. Perdew, K. Burke, and M. Ernzerhof, Phys. Rev. Lett. **77**, 3865 (1996).

[55] A. van de Walle, P. Tiwary, M. de Jong, D. L. Olmsted, M. Asta, A. Dick, D. Shin, Y. Wang, L.-Q. Chen, and Z.-K. Liu, Calphad **42**, 13 (2013).